The Astrophysical Journal, 884:158 (8pp), 2019 October 20 https://doi.org/10.3847/1538-4357/ab426e

The Variability of Solar Coronal Abundances in Active Regions and the Quiet Sun

G. A. Doschek[1] and H. P. Warren[2]
[1] Voluntary Emeritus Program, Space Science Division, Naval Research Laboratory, Washington, DC 20375, USA
[2] Space Science Division, Naval Research Laboratory, Washington, DC 20375, USA
Received 2019 July 9; revised 2019 September 4; accepted 2019 September 5; published 2019 October 22

Abstract

Measurements of elemental abundances hold important clues to how mass and energy flow through the solar atmosphere. Variations in abundances are organized by an element's first ionization potential (FIP), and many previous studies have assumed that low FIP (less than 10 eV) elements are enriched by a factor of 3–4 in the corona. In this paper, we use spatially resolved observations from the Extreme-ultraviolet Imaging Telescope on board the *Hinode* spacecraft to examine the spatial variability of elemental abundance in and around active regions. We find substantial variations within some active regions. In general, however, we find that the enrichment of low FIP elements is limited to bright, active region structures. In faint active region structures and in the dark, quiet regions around active regions, the measured abundances are close to photospheric. These measurements use the ratio of low FIP Si to high FIP S. Similar conclusions concerning quiet Sun regions have been reached recently by Del Zanna using full-Sun spectra. He has found that the coronal quiet Sun (at temperatures greater than 1 MK) has photospheric abundances. Transition region abundances (at temperatures less than 1 MK in the solar atmosphere) have been found to be photospheric. These results and results from this paper suggest that a coronal composition is not a general property of million-degree plasma, but is limited to bright active region loops, and is variable.

Key words: Solar abundances – Solar corona

1. Introduction

The elemental abundances in the corona have been discussed extensively since about 1985 (e.g., Meyer 1985a, 1985b; Feldman 1992; Schmelz et al. 1996, 2012; Del Zanna 2013b; Del Zanna & Mason 2014; Reames 2014). Elemental abundances in the solar atmosphere are also discussed in the solar spectral diagnostics compendia by Phillips et al. (2008) and Del Zanna & Mason (2018). It was found that the abundances in the corona could be significantly different than in the photosphere, and perhaps a bit variable. It was concluded that elements with a first ionization potential (FIP) less than 10 eV are in many measurements more abundant in the corona by a factor of 3–4 than in the photosphere. It has been generally assumed that elements with an FIP greater than 10 eV have the same abundance in the corona as in the photosphere. The measurements cited above have been made in several ways using X-ray and extreme-ultraviolet spectral lines. The overall results are consistent with in situ measurements of solar energetic particles.

Rather recently, Doschek et al. (2015), Doschek & Warren (2016, 2017), and Baker et al. (2018, 2019) investigated small regions on the Sun that reflected an inverse FIP effect, i.e., regions where the coronal abundances of low FIP elements are less than in the photosphere while the high-FIP elements remain with photospheric abundances. Evidence that the low FIP elements are in fact enhanced in the corona and not depleted is discussed in Doschek & Warren (2016). So far, these regions are only found near sunspots. Near sunspots, the normal FIP effect may in some cases lessen or shut down, producing extensive coronal regions with photospheric abundances and very small regions with inverse FIP abundances (Doschek & Warren 2017).

The best theory for the FIP effect known to the authors has been proposed by Laming (2004, 2015). In this model, a ponderomotive force produced in waves, e.g., Alfvén waves, can sweep low FIP elements up into the corona, increasing their abundances relative to the high-FIP elements. The model also predicts a downward pointing ponderomotive force in some cases, where low FIP coronal elements are pushed down into the chromosphere. This is the inverse FIP effect and occurs preferentially near sunspots. Some stars have extremely large starspots that cover a substantial fraction of their surfaces. In these stars, the average coronal spectrum exhibits the inverse FIP effect (e.g., Vogt & Penrod 1983; Drake et al. 2001; Wood et al. 2012; Wood & Laming 2013). An important prediction of the Laming (2015) model is that the FIP effect should vary in the corona, reflecting the complexity of magnetic fields in the chromosphere.

In this paper, we primarily study the ratio of a low FIP line of Si X(258.375 Å) to what we assume is a high-FIP ion of S X (264.233 Å). This ratio has been examined for quiet Sun and active region abundance measurements (e.g., Brooks et al. 2015; Baker et al. 2018). In active regions, the emission comes primarily from closed loops. The Laming (2015) model predicts that sulfur will behave as a high-FIP element in closed loops (e.g., Laming et al. 2019). We calculate the FIP effect by comparing measured line ratios in active regions and surrounding quiet Sun regions with the computed ratio in the photosphere using photospheric abundances of Si and S (Caffau et al. 2011). The Si X/S X FIP effect depends on both electron temperature and density. We determine a density estimate using the Fe XIII(202.044)/Fe XIII (203.826 Å) line ratio. We estimate temperatures using the Fe XI (188.216+188.299 Å)/Fe XII(192.394 Å) line ratio. These ions cover a range of coronal temperatures from about 1.2 to 4.5 MK. The spectra are from the Extreme-ultraviolet Imaging Spectrometer (EIS) raster scans of active regions obtained from the *Hinode* spacecraft. Our adopted abundances and atomic data are the same as those given in Doschek & Warren (2017).

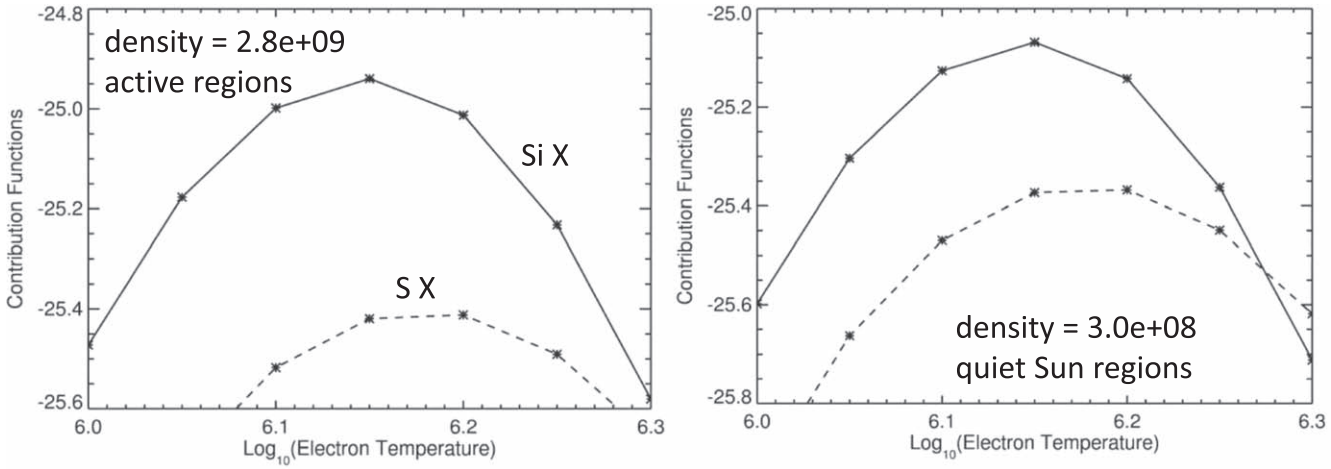

Figure 1. Photospheric abundance contribution functions shown for two electron densities for Si X and S X. These densities are close to the averages of all of the measured densities in the active region and quiet Sun regions.

Table 1
Active Regions Observed

Date	Start Time (UT)	EIS file
2011 Mar 29	09:42	eis_l1_20110329_094224
2011 Apr 01	09:55	eis_l1_20110401_095455
2011 Apr 15	00:15	eis_l1_20110415_001526
2012 Mar 29	15:01	eis_l1_20120329_150130
2013 Dec 26	10:32	eis_l1_20131226_103129
2013 Dec 28	11:11	eis_l1_20131228_111038
2013 Dec 29	10:51	eis_l1_20131229_105059
2014 Jan 08	09:57	eis_l1_20140108_095727
2014 Jan 11	10:26	eis_l1_20140111_102621
2014 Jan 25	10:33	eis_l1_20140125_103334
2014 Feb 01	10:50	eis_l1_20140201_105035
2014 Feb 02	10:25	eis_l1_20140202_102527
2014 Feb 03	09:31	eis_l1_20140203_093134
2014 Feb 05	10:41	eis_l1_20140205_104127
2014 Dec 15	10:26	eis_l1_20141215_102603
2014 Dec 17	22:18	eis_l1_20141217_221744
2015 Dec 10	10:50	eis_l1_20151210_104940
2016 Feb 13	12:32	eis_l1_20160213_123147
2016 Feb 14	11:21	eis_l1_20160214_112035
2016 Feb 15	10:34	eis_l1_20160215_103336
2016 Feb 19	11:57	eis_l1_20160219_115659
2016 Feb 20	03:04	eis_l1_20160220_030429

2. The EIS Spectrometer and Data Reduction

The EIS spectrometer is described by Culhane et al. (2007). EIS observes within two wavelength bands between about 170–213 Å and 250–290 Å. The instrument consists of a telescope that produces an image on a selected spectrometer slit, oriented in the north–south direction. Spectra are formed on two CCD detectors. Up to 25 spectral lines can be observed in selected wavebands centered on a spectral line of interest, or a full-CCD spectrum can be selected, i.e., the entire wavebands of both CCDs are recorded. Rasters obtained by EIS are scans from west to east.

The EIS data are processed using standard EIS software for dark current, the CCD pedestal, warm pixels, slit tilt, and temperature variations due to the *Hinode* orbit. We continue using the old EIS calibration instead of the new calibrations discussed by Del Zanna (2013a) or Warren et al. (2014). We concentrate on detecting systematic differences in spectra among different solar regions. This is independent of the calibration used, but the calibration is not important in any case since all of the line ratios involve two lines close in wavelength.

We examine data obtained using the raster study, HPW021_vel_240x512v1. We examine 22 active regions and revisit the active region with large sunspots that was observed using full-CCD spectral rasters and discussed in Doschek & Warren (2017). The data for this region that we discuss were obtained using the HPW021 study. The HPW021 study uses the 1″ slit, but rasters are made with a 2″ step size. The size of the rasters is 240″ × 512″. Twenty-five lines are observed by this study, each with a 60 s exposure. Each raster of an active region includes quiet Sun regions. However, the quiet Sun regions are limited in observed area and may contain weak active region emission. The dates and start times of observations are listed in Table 1.

3. Observations

Si X and S X are both formed at about 1.5 MK, but the Si X/S X intensity ratio is sensitive to the electron density and temperature of the emitting plasma. Therefore, observations of these quantities are necessary for calculating an FIP effect from the Si X/S X ratio. Figures 1 and 2 show the effect of density and temperature on the contribution functions of Si X and S X. The atomic data are from Young & Landi (2009; CHIANTI). The results are for two densities. These densities are close to the averages of all of our densities measured in the 22 active regions and surrounding dark Sun regions. The difference between active regions and quiet Sun regions is about an order of magnitude.

Inspection of Figures 1 and 2 shows that as the density decreases, the Si X/S X ratio also decreases. Interpreted incorrectly as an FIP effect, this would imply that lower-density regions have closer to photospheric abundances than high-density regions. Contrary to this, a decrease of temperature results in an increase of the Si/S intensity ratio, incorrectly implying a larger FIP effect for lower temperatures. To account for the temperature and density sensitivity, we developed a program that takes the temperature and density as inputs and outputs the Si/S ratio assuming photospheric abundances. This ratio is compared with the observed ratio to produce the FIP bias. A value of 1 corresponds to a photospheric composition.

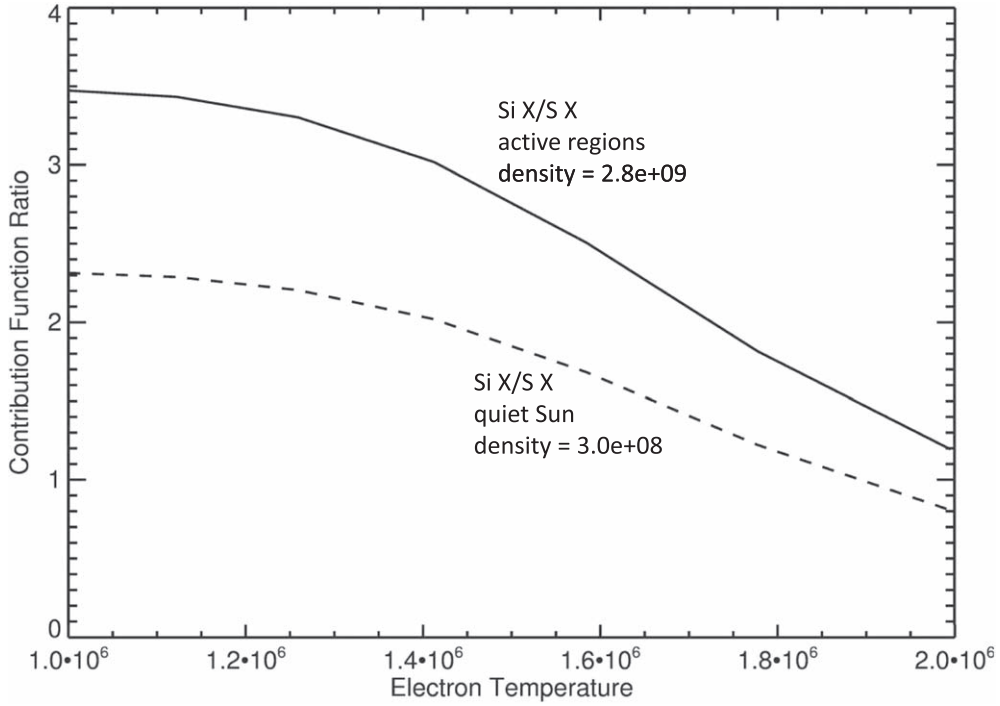

Figure 2. The Si X/S X intensity ratio (in energy units) for the densities discussed in Figure 1.

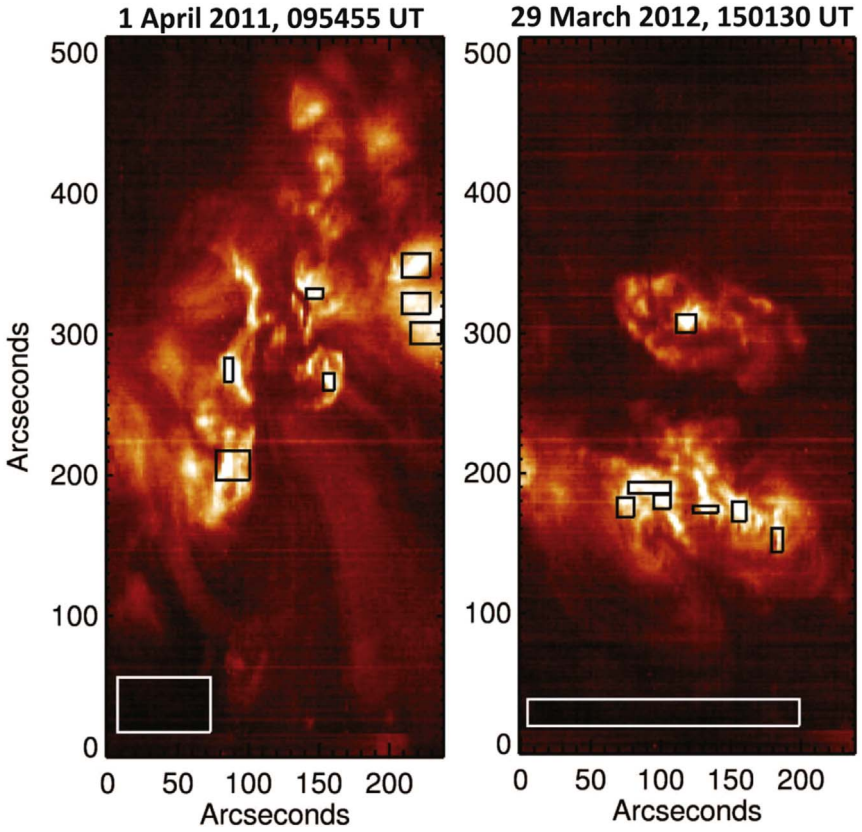

Figure 3. Two sample active regions illustrating areas where average temperatures, densities, and FIP effects were determined. The Si X line was used to make the images. There are seven regions (black boxes) obtained in bright areas for each active region, and one quiet Sun region (white box) recorded in a dark region close to the bright areas.

In order to obtain the input line ratios, densities, and temperatures, a program was written that can select a number of spatial regions of any square or rectangular size in an EIS active region image and sum up all of the relevant spectroscopic quantities over each region to produce an average spectrum for the region with high statistics in the line intensity

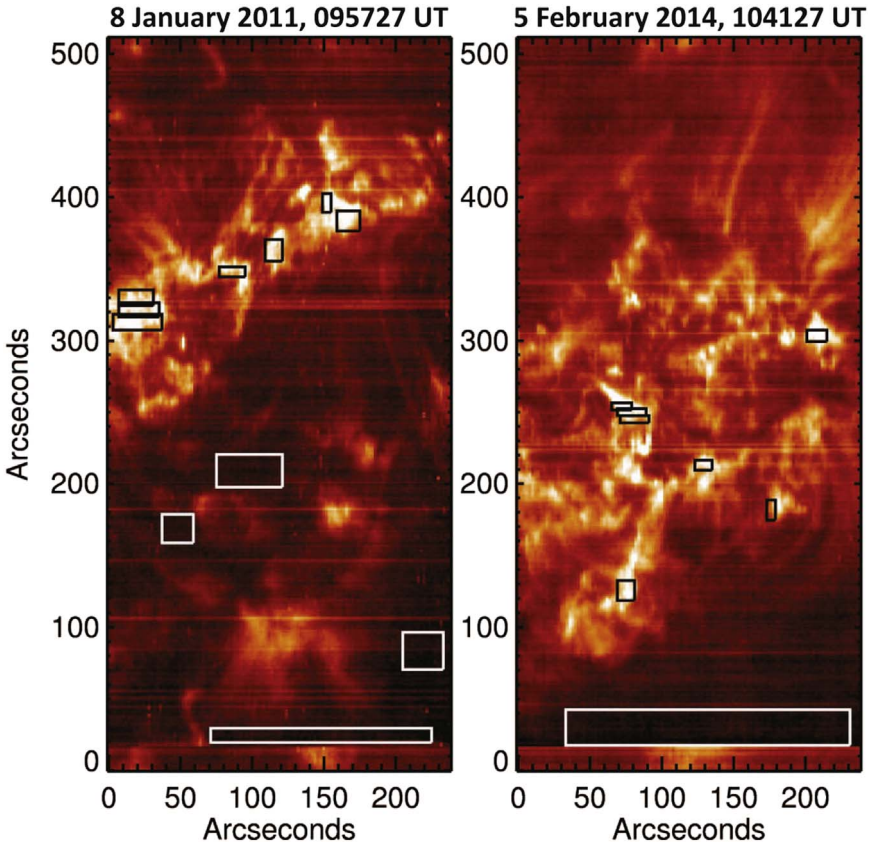

Figure 4. Two active regions that show a large FIP effect (left panel) and an inverse FIP effect (right panel). The Si X line was used to make the images. Several quiet Sun regions are shown in the left plot in areas where on a log plot, no significant emission can be detected by eye.

measurements. The EIS data for each line are obtained in wavelength windows of variable size. A continuum region is chosen and a continuum is substracted from each window before determining the line intensity. The Fe XIII line at 203 Å is blended with another line. For this line, a two-Gaussian fit is made to the line to determine the Fe XIII intensity. The summed spectra of Si X, S X, Fe XIII 202, and Fe XIII 203 Å lines are displayed and visually inspected for each small region chosen within the active region. Typically, seven regions are chosen for each active region. It is more difficult choosing quiet Sun regions. We chose quiet Sun regions that appear completely dark in log images of the active regions. Since the statistics in these regions are much less than in the bright active regions, we preferred large dimensioned quiet Sun areas to improve the statistics. Sample active region plots with chosen regions are shown in Figures 3 and 4.

4. Results

We show in detail in Tables 2–5 results from the four different active regions shown in Figures 3 and 4. There are four quiet Sun regions for the January 8 event shown in Figure 4 and one quiet Sun region for the other three active regions. There are seven locations in the bright active region areas for all four examples shown in Figures 3 and 4. These are always shown first in the tables. The last region in the tables is always a dark or quiet Sun region. The tables contain the central pixels of each box. For example, for the April 1 event (left panel of Figure 3), the position 219,349 is the central abscissa and ordinate pixels for the top-most box in the figure. The other quantities are self-explanatory. The densities and temperatures refer to electrons, and the line ratio is in ergs, not photons.

Table 2
The 2011 April 1 Active Region

Position	FIP bias	Density	Temperature	Si X/S X Ratio
219,349	1.84	9.07	6.20	4.07
219,322	2.13	8.99	6.19	4.69
226,301	2.14	8.89	6.18	4.84
147,329	2.81	9.37	6.22	6.08
86,275	2.08	9.28	6.22	4.43
157,266	1.97	9.41	6.21	4.48
89,207	1.92	9.22	6.22	4.09
40,37	1.31	8.39	6.21	2.00

Table 3
The 2012 March 29 Active Region

Position	FIP bias	Density	Temperature	Si X/S X Ratio
118,307	1.76	9.39	6.22	3.73
183,152	1.91	9.23	6.20	4.44
156,172	2.31	9.37	6.20	5.50
132,174	1.53	9.44	6.21	3.63
101,180	1.88	9.37	6.21	4.29
92,190	1.84	9.35	6.21	4.13
75,175	1.89	9.20	6.20	4.25
102,29	1.29	8.45	6.17	2.40

All of the tables show considerable variability in the FIP bias. The statistics of the line intensities in the bright regions are quite good, so this variability is real. Note that the FIP

Table 4
The 2011 January 8 Active Region

Position	FIP bias	Density	Temperature	Si X/S X Ratio
152,396	2.72	9.55	6.21	6.74
167,383	3.13	9.47	6.20	7.73
114,363	2.78	9.71	6.20	7.35
86,348	2.80	9.75	6.20	7.45
20,323	3.54	9.51	6.20	9.15
20,321	3.77	9.47	6.20	9.73
20,330	3.59	9.40	6.20	9.08
220,83	1.00	8.63	6.22	1.66
74,48	1.20	8.69	6.21	2.07
98,209	1.23	8.91	6.24	2.05
48,169	1.49	8.82	6.22	2.70

Table 5
The 2014 February 5 Active Region

Position	FIP bias	Density	Temperature	Si X/S X Ratio
80,245	0.80	9.81	6.22	2.04
80,250	0.77	9.82	6.21	2.07
72,254	0.80	9.81	6.20	2.28
208,304	2.40	9.67	6.20	6.29
130,213	2.10	9.69	6.21	5.40
176,181	1.75	9.26	6.21	3.93
75,125	1.66	9.55	6.22	3.69
132,30	1.55	8.48	6.22	2.35

biases for the dark regions are all small, about 1.5. In general, dust on the slit can interfere considerably with FIP biases in regions where the line intensities are quite low. The quiet Sun FIP biases are generally around unity, i.e., photospheric, or slightly above photospheric.

A comparison of the bright active region electron densities with the dark region densities in Tables 2–5 shows that the bright region densities are about an order of magnitude greater than the dark region quiet Sun densities, although there is a lot of variation. This result is the same as found for all of the active and quiet Sun regions that we have examined.

The temperatures in Tables 2–4 are about what is expected for all of the spectral lines we are using. The active region and quiet Sun temperatures are about the same.

It will be seen later that for all of the active regions, the Si X/S X line intensity ratio variations and the FIP bias variations are on average quite similar, showing that the Si/S line ratio is the most important parameter in determining the FIP biases. In Figure 4, the active region FIP biases (bright regions) for the January 8 active region (Table 4) are all above two, and four of the measurements have values greater than three. An FIP bias of three or more is unusual. This active region resembles the expected results from the previous FIP studies mentioned in the introduction. The FIP bias for all of the dark quiet Sun regions is less than two.

The March 29 active region (Table 3) shows results that are quite different from the January 8 region. This active region has FIP biases close to two, and none that are even close to three. The results for electron density and temperature are similar to the results for the January 8 active region just discussed. (The densities are slightly lower in the March 29 region.) The quiet Sun FIP bias is not quite photospheric although the difference is small.

Finally, the February 5 active region shown in Table 5 shows some unusual results. The FIP biases for the first three entries are less than one, even though the electron densities are quite high. Each of these regions is a bright region, but the FIP bias is less than those found for the dark quiet Sun regions, which have much lower densities. This event has been discussed by Doschek & Warren (2017). The first three regions in Table 5 are areas with a strong inverse FIP effect, and the Si/S ratio is simply showing the same effect as found for other spectral line ratios obtained for this active region.

We show more data for the February 5 active region as color maps in Figure 5. The regions selected are not all the same as in Figure 4. These color maps show FIP biases, densities, temperatures, and observed Si/S lines ratios that are generally consistent with the values in Tables 2–5. The theoretical Si/S ratio obtained assuming photospheric abundances is shown compared with the observed Si/S ratio. The ratio of these maps is the FIP bias. The inverse FIP region just discussed is clearly seen in the FIP map shown in Figure 5.

5. Discussion

The results for all of the active regions are shown in Figure 6. The stars represent active region values, and triangles indicate a few quiet Sun values shown in the FIP bias and electron density plots. The averages of all of the quantities for the 22 active regions examined are: log density active regions = 9.47, quiet Sun = 8.50; log temperature active regions = 6.20, quiet Sun = 6.20; Si/S line intensity ratio active regions = 5.03, quiet Sun = 2.66; FIP bias active regions = 2.07, quiet Sun = 1.52. There are some quiet Sun regions with FIP biases greater than two that were discarded because of dust on the slit or other data problems. In addition, for the quiet Sun data, all of the quiet Sun regions from the active region shown in the left panel of Figure 4 are included. As mentioned, for quiet Sun regions, the data can easily be corrupted because of the low intensities and dust on the slit. The quiet Sun FIP biases that we obtain are closer to photospheric than the active region biases, which we believe are displaying an FIP effect. In addition, the quiet Sun regions we examine are close to active regions and may contain some active region emission. The active region densities are on average eight times larger than the quiet Sun densities, about as expected.

Note the active region FIP biases in the upper left panel that are below or close to one. The FIP biases are close to photospheric or less than photospheric, but all of the densities for these particular FIP biases are high active region densities, and the regions are bright, not dark. As mentioned, these FIP biases are from areas in the 2014 February sunspot active region discussed in Doschek & Warren (2017) that exhibit inverse FIP characteristics at the higher temperatures where Ar XIV and Ca XIV are formed, as well as for lower-temperature regions where Ar XI and S XI are formed. Figure 6 shows that the inverse FIP condition also holds for Si X and S X, as expected. The Doschek & Warren (2017) paper on this region dealt with full-CCD scans, complementing the data obtained with the HPW021 study. The lowest FIP biases in Figure 6 (0.77, 0.80) come from the scan on 2014 February 5 (Table 5). The FIP biases near 1 come from an earlier scan on 2014 February 3 (Table 1).

There is considerable variability in the active region FIP biases within some regions, but the average FIP bias of our

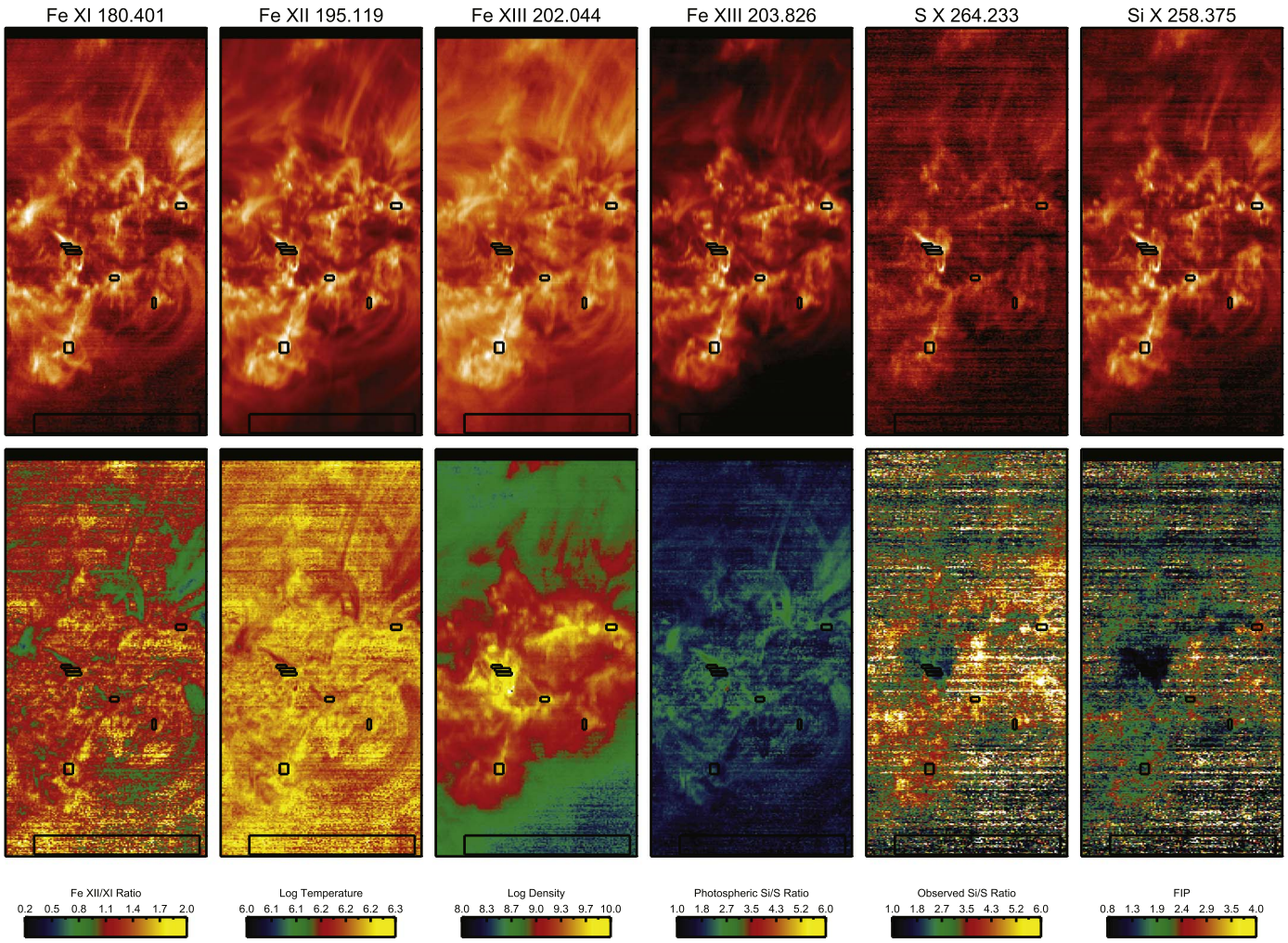

Figure 5. A color map showing intensities, Fe XII/Fe XI intensity ratios, temperatures, densities, photospheric Si X/S X ratios, observed Si X/S X ratios, and FIP biases, for selected areas in the February 5 event.

measurements in many of the active regions is close to 2. There is no relationship between the FIP bias and the ages of the active regions. Dahlburg et al. (2016) predicts from numerical simulations that the FIP effect is a consequence of coronal heating. It occurs ubiquitously in coronal loops heated by nanoflares. Variations in loops and the physical conditions and magnetic fields within the loops would be responsible for the FIP variations we see.

But how real is this, and what are the uncertainties involved? The statistical uncertainties in the line intensities are negligible because we chose boxes and added all of the intensities, reducing statistical uncertainties to very small values. There may be a few problems with some of the active region spectra added that affect the final line intensities, due to, for example, dust on the slit, but these uncertainties are small. The magnitude of the uncertainties in the ionization equilibrium calculations is unknown. Much of the ionization equilibrium data have never been verified by laboratory measurements. Almost all other atomic data in astronomy are in a similar situation. The same type of statement applies to collisional excitation rates and spontaneous radiative decay rates for spectral lines. Laboratory measurements are difficult and time-consuming. However, we are most interested in variations, not precise FIP biases. The atomic data we use are the same for all of the measurements and so should not produce the variations we observe.

Figures 1 and 2 imply sensitivity to both density and temperature. So, could the FIP variations simply reflect variations of these parameters? We have calculated correlation coefficients between the active region FIP measurements and density, temperature and the Si/S line intensity ratio. The correlations of FIP bias with density and temperature are near zero for the active regions. Only the correlation of FIP bias with line ratio is significant for the active regions (0.94). All of our results show that the variations we see are due primarily to line intensity variations, which imply abundance variations.

Another source of uncertainty is degradation of the EIS instrument with time due to contamination. This uncertainty should be small because all of the line pairs from which ratios are obtained are close together in wavelength. Therefore, variation of contamination with wavelength is unlikely to be significant. All of the data in Figure 6 is ordered chronologically from 2011 through 2016 and none of the ratios show gradual increases or decreases in line ratios that might indicate uneven contamination.

Examination of Figure 6 shows that FIP biases of about three are relatively rare, and from the FIP bias data, it is clear that some active regions have much higher FIP biases than other

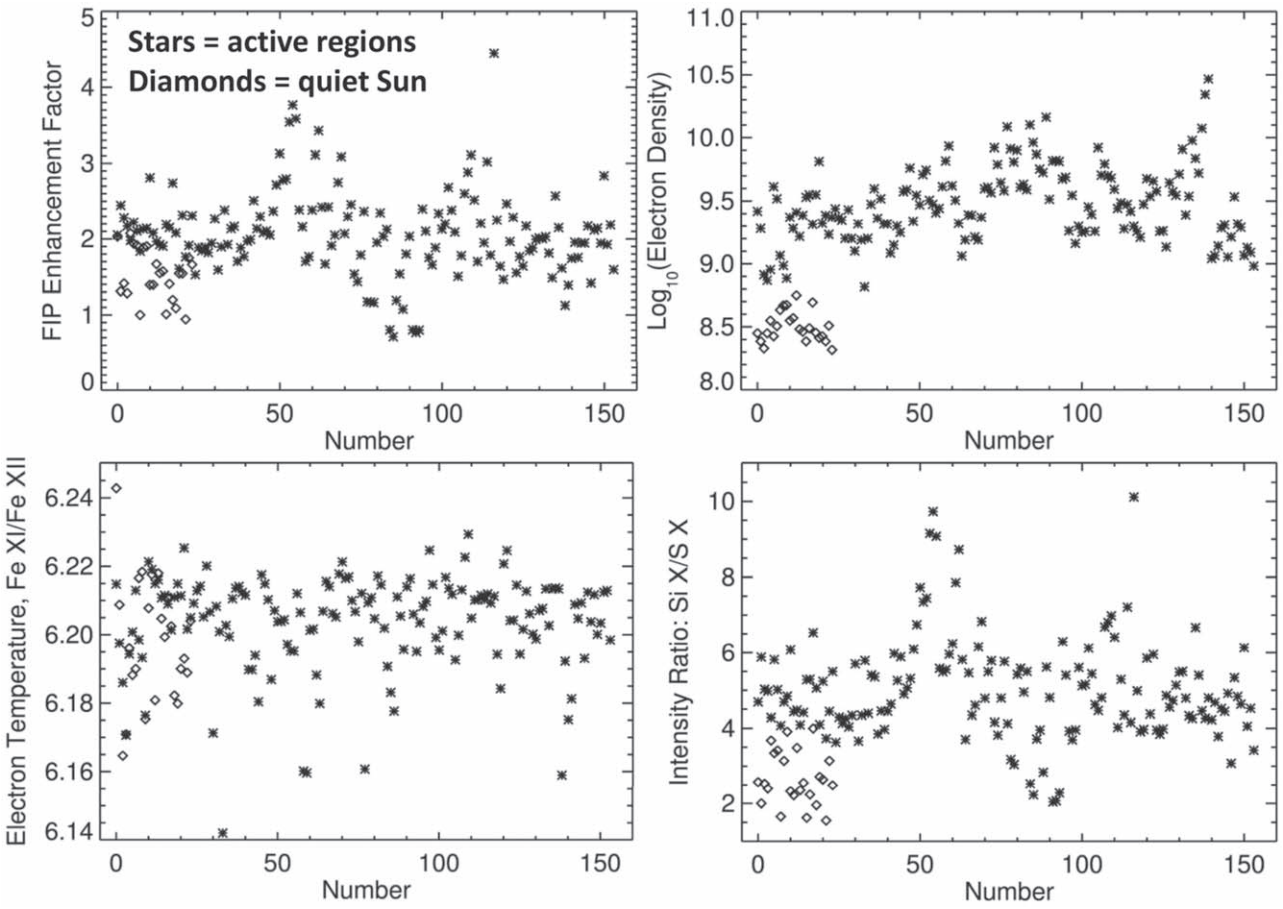

Figure 6. Results for all 22 active regions. All of the Si/S FIP bias factors, electron densities determined from the Fe XIII line ratio, temperatures determined from the Fe XI/Fe XII ratio, and the Si X/S X intensity ratios, are shown for all of the measurements in each active region and in surrounding quiet Sun regions.

regions. The largest FIP biases come from the active region shown in Figure 4.

Figure 6 shows that a new picture is now emerging concerning coronal abundances. The earlier measurements referenced above noted that different types of solar structures could have very different abundances, but it was generally assumed that active regions constitute one type of region with an FIP effect of about 3–4. Now we have found that although the FIP effect is present primarily in active regions, it can vary considerably from one active region to another and within an active region. This is generally expected in the Laming (2015) model, but the model does not predict the extent of the variability.

We find that the quiet coronal Sun has close to photospheric abundances, but perhaps a little enhanced. The dark regions we have chosen are quite close to the active regions, and the FIP biases we find for dark regions may be enhanced because of this proximity. In general, however, our results qualitatively support a quiet Sun abundance close to photospheric, as found by Del Zanna (2019). This is in apparent contradiction with the results of Laming et al. (1995), who found that the FIP effect apparently increases with temperature, with no FIP effect at transition region temperatures, but an FIP effect at coronal temperatures (above 10 MK). This is probably due to Laming et al. (1995) using full-disk data obtained by Malinovsky & Heroux (1973), as opposed to the ability now to select small solar regions for analysis. The Malinovsky & Heroux (1973) spectrum has an active region component, which could explain the coronal abundance obtained by Laming et al. (1995). The Del Zanna (2019) full-disk spectrum was obtained during a solar minimum period. The precise value of the FIP effect may depend on the element and is still somewhat uncertain due to uncertainties in atomic data. The assumption that high-FIP element abundances in the corona and chromosphere are the same as in the photosphere is still not verified.

The abundances in the corona, chromosphere, and photosphere are important for several reasons. The abundance variations can be used to trace fast and slow solar wind. Values of the abundances are important for radiative loss calculations in coronal models such as flare loop models. But the really important reason for studying abundances is that they depend critically on wave motion in the chromosphere and how it interfaces with the corona. The corona may be heated at least in part by waves, and the abundance variations in the corona and chromosphere are indicators of the wave variations between the corona and chromosphere. It seems that the wave motions and types of waves in the chromosphere depend on the presence of sunspots in active regions and possible mode changes of the waves due to the more intense sunspot magnetic fields.

A dedicated solar element abundance space experiment seems to be the next step in investigating solar coronal abundances in detail.

Hinode is a Japanese mission developed and launched by ISAS/JAXA, collaborating with NAOJ as a domestic partner, and NASA (USA) and STFC (UK) as international partners. Scientific operation of the *Hinode* mission is conducted by the

Hinode science team organized at ISAS/JAXA. This team mainly consists of scientists from institutes in the partner countries. Support for the post-launch operation is provided by JAXA and NAOJ, STFC, NASA, ESA (European Space Agency), and NSC (Norwegian Space Center). We are grateful to the *Hinode* team for all of their efforts in the design, build, and operation of the mission.

H.P.W. acknowledges support from the NASA *Hinode* program. G.A.D. thanks support from the NRL Voluntary Emeritus Program. We thank Dr. Martin Laming for helpful comments on the manuscript.

ORCID iDs

G. A. Doschek https://orcid.org/0000-0002-7625-9866
H. P. Warren https://orcid.org/0000-0001-6102-6851

References

Baker, D., Brooks, D. H., van Driel-Gesztelyi, L., et al. 2018, ApJ, 856, 71
Baker, D., van Driel-Gesztelyi, L., Brooks, D. H., et al. 2019, ApJ, 875, 35
Brooks, D. H., Ugarte-Urra, I., & Warren, H. P. 2015, NatCo, 6, 5947
Caffau, E., Ludwig, H.-G., Steffen, M., Freytag, B., & Bonifacio, P. 2011, SoPh, 268, 255
Culhane, J. L., Harra, L. K., James, A. M., et al. 2007, SoPh, 243, 19
Dahlburg, R. B., Laming, J. M., Taylor, B. D., & Obenschain, K. 2016, ApJ, 831, 160
Del Zanna, G. 2013a, A&A, 555, A47
Del Zanna, G. 2013b, A&A, 558, A73
Del Zanna, G. 2019, A&A, 624, A36
Del Zanna, G., & Mason, H. E. 2014, A&A, 565, A14
Del Zanna, G., & Mason, H. E. 2018, LRSP, 15, 5
Doschek, G. A., & Warren, H. P. 2016, ApJ, 825, 36
Doschek, G. A., & Warren, H. P. 2017, ApJ, 844, 52
Doschek, G. A., Warren, H. P., & Feldman, U. 2015, ApJL, 808, L7
Drake, J. J., Brickhouse, N. S., Kashyap, V., et al. 2001, ApJL, 548, L81
Feldman, U. 1992, PhyS, 46, 202
Laming, J. M. 2004, ApJ, 614, 1063
Laming, J. M. 2015, LRSP, 12, 2
Laming, J. M., Drake, J. J., & Widing, K. G. 1995, ApJ, 443, 416
Laming, J. M., Vourlidas, A., Korendyke, C., et al. 2019, ApJ, 879, 124
Malinovsky, L., & Heroux, M. 1973, ApJ, 181, 1009
Meyer, J.-P. 1985a, ApJS, 57, 173
Meyer, J.-P. 1985b, ApJS, 57, 151
Phillips, K. J. H., Feldman, U., & Landi, E. 2008, Ultraviolet and X-ray Spectroscopy of the Solar Atmosphere (Cambridge: Cambridge Univ. Press)
Reames, D. V. 2014, SoPh, 289, 977
Schmelz, J. T., Reames, D. V., von Steiger, R., & Basu, S. 2012, ApJ, 755, 33
Schmelz, J. T., Saba, J. L. R., Ghosh, D., & Strong, K. T. 1996, ApJ, 473, 519
Vogt, S. S., & Penrod, G. D. 1983, PASP, 95, 565
Warren, H. P., Ugarte-Urra, I., & Landi, E. 2014, ApJS, 213, 11
Wood, B. E., & Laming, J. M. 2013, ApJ, 768, 122
Wood, B. E., Laming, J. M., & Karovska, M. 2012, ApJ, 753, 76
Young, P. R. 2005, A&A, 439, 361
Young, P. R., & Landi, E. 2009, ApJ, 707, 173